AERODYNAMIC CHARACTERISTICS OF A LIFT- FAN UNDER LARGE INFLOW DISTORTION FOR V/STOL APPLICATIONS

N. Thouault, C. Breitsamter and N.A. Adams
Institute of Aerodynamics, Technische Universität München
Boltzmannstrasse 15, D-85748 Garching
Germany

Abstract

The present investigation focuses on the analysis of the aerodynamic characteristics of a lift-fan under large inflow distortion in the form of a fan-in-wing configuration. The flow distortion at the fan inlet is investigated for a generic wind tunnel model, using unsteady computational fluid dynamics results. Due to the specific arrangement of the fan being installed in the wing, flow separation occurs on the inlet lip and generates a recirculation bubble above the rotor blades. A distortion of the total pressure distribution at the fan inlet significantly influences the blade loading. The strong flow acceleration over the inlet lip induces an increase of the axial velocity component and results in a reduction of incidence angle on the rotor blade. In the bubble core region, the low axial velocity component enhances the blade incidence angle and provokes blade tip stall. Steady Reynolds Averaged Navier-Stokes calculations, using an actuator disk approach, are then conducted to identify the key parameters affecting lip boundary layer separation. The speed ratio and the ratio of inlet lip radius to diameter influence the total pressure distribution at the fan inlet by modifying the location of the flow separation. The angle of attack on the wing has a negligible impact on the inflow distortion. An inlet guide vane located in the vicinity of the inlet lip contributes to reduce the extension of the recirculation bubble but requires to be adjusted adequately to the operating conditions to avoid vane stall.

Nomenclature

α Wing angle of attack, deg
α_i Duct inlet vane angle, deg
γ Swirl angle, deg
ϕ Flow coefficient, $Q/(nD^3)$
θ Circumferential position, deg
θ_v Guide vane circumferential position, deg
ρ Density, kg/m^3
ψ Pressure rise coefficient, $\Delta Ps/(\rho\, n^2\, D^2)$
τ Torque coefficient, $M/(\rho\, n^2\, D^5)$
b Wing span, m
c Wing root chord, m
C_T Thrust coefficient, $T/(\rho\, n^2\, D^4)$
D Fan diameter, m
l_{max} Maximum radial length of the separation bubble, m
M Fan torque, N.m
n Fan rotational speed, rps
N Fan rotational speed, rpm
Ps Local static pressure, Pa
Ps_∞ Freestream static pressure, Pa
Pt Local total pressure, Pa
Pt_∞ Freestream total pressure, Pa
Q Mass flow through the fan, kg/s
r Radial position, m
r_v Guide vane radial position, m
r_{lip} Lip radius, m
R Fan radius, m
Re_c Reynolds number based on the wing root chord
t Wing maximum thickness, m
T Fan thrust, N
U_t Rotor tip speed, m/s
V_∞ Freestream velocity, m/s
V_a Axial velocity component, m/s
V_c Circumferential velocity component, m/s
V_j Jet velocity, m/s
z Axial position, m
AVG Time-averaged results over 1 fan revolution
CFD Computational Fluid Dynamics
IGV Inlet Guide Vane
REF Reference, fan alone without inlet distortion
TRN Instantaneous results
URANS Unsteady Reynolds Averaged Navier-Stokes
V/STOL Vertical/ Short Take Off and Landing

1. INTRODUCTION

Vertical and Short Take-Off and Landing aircraft can be an alternative for short to medium range aircraft, to relieve congestion on airports and face the increase in air transportation traffic [1]. The lift-fan is a potential solution to provide additional lift for V/STOL capability [2]. For example, a lift-fan was contained in the wing of the Ryan GE XV-5A fan-in-wing NASA experimental aircraft to offer hovering ability. A lift-fan is also currently used in the F-35B fuselage for longitudinal stability purposes. A large amount of experimental and numerical investigations have been undertaken to study the effects of inlet distortion on the performance of axial compressors. Non-uniform inflow can induce compressor stall or surge resulting in a significant drop of efficiency. The main sources of distortions, related to each other, are the total pressure, the total temperature and the swirl distortions [3]. The effect of inlet circumferential distortion in a transonic compressor rotor was studied by Hah et al. [4]. The

distortion travels through the rotor blade passage and can affect the stator. Pressure distortion can induce a swirl distortion that is transmitted through the blade passage in multistage fans [5]. Inflow distortion can be generated at the compressor inlet due to specific installation. For example, the shape of the hub-cap [6] or the nacelle droop [7] can be a source of distortion. The non-uniform inflow distribution is a critical issue for fighter aircraft at high angle of attack [8]. Flow separation can occur on the engine intake lip and can strongly affect the inlet total pressure distribution. For V/STOL aircraft, inflow distortion is also a major problem. For example, a large recirculation area can be generated on the nacelle droop of a tilt-nacelle aircraft at severe freestream conditions [9]. The inlet distortion is also critical for an axial fan installed orthogonally to the freestream direction and can possibly cause an excitation of the fan at its natural frequency and provoke significant damage. On the F-35B under cross-flow condition, separation can occur on the bellmouth inlet affecting considerably the flow angularity and total pressure distribution at the lift-fan inlet section [10]. In this study, the design of the inlet lip is of major interest to reduce the total pressure distortion. For a fan-in-wing configuration in transition flight out-of-ground effect, a non-uniform swirl angle distribution is observed, aggravating the noise level [11]. Regarding cruise performance, the fan has to be housed compactly thereby imposing significant fan design constraints. The inflow depth and the inlet lip shape are parameters influencing the inlet total pressure and swirl distortions [12]. For fan-in-wing configurations, guiding vanes above the fan inlet can improve the flow ingestion [13-16]. Inlet guide vanes are also used for various V/STOL applications, as for example a lift-fan fitted in a nacelle [17]. However, the inlet guide vane wake impinges on the rotor causing a spatial non-uniform velocity distribution [18]. In a previous study, the aerodynamic characteristics of a generic fan-in-wing configuration were analyzed (Fig. 1). The situation studied reflects a transition flight out-of-ground effect. A generic wind tunnel model was build and the performance of the wing with various fan arrangements was analyzed [19]. A configuration, with a single fan located at the rear part of the wing has been reproduced numerically. These numerical results are in satisfying agreement with various experimental data for the wing aerodynamics [20].

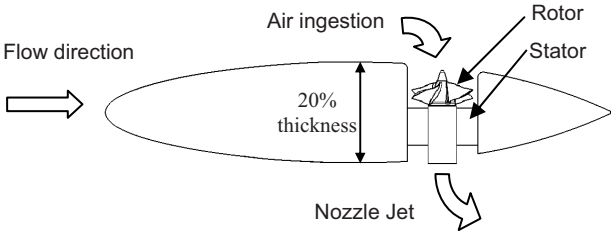

FIG 1. Schematic view of the experimental setup

As previously stated, distortion due to inlet lip separation appears in a wide range of V/STOL configurations. However, a number of questions remain open concerning the flow characteristics at the fan inlet (e. g. velocity and total pressure distributions), useful for the design of such lift-fans. All the previous fan-in-wing investigations are experimental and provide limited access to the flow topology and the configuration behavior. The use of state-of-the-art CFD methods can contribute to provide further information on the flow properties of a lift-fan being installed in a wing and can allow a large spectrum of parameter variation.

In the present study, the total pressure and swirl inlet distributions at the fan inlet will be analyzed using a URANS approach. The aerodynamic characteristics of the lift-fan integrated in the wing will be compared to steady results of the fan-alone without inlet distortion. Then, using an actuator disk approach to model the fan, the main parameters affecting the inlet total pressure distortion will be documented. This study intends to increase the design sensitivity of lift-fan subjected to inlet distortion often encountered in V/STOL applications.

2. DISTORTION CHARACTERISTICS

Using time-averaged URANS results of the entire generic wind tunnel model geometry [20], the aerodynamic characteristics of the inflow distortion are described and compared to a simulation of the fan without distortion.

2.1. Wind tunnel model description

The model airfoil is of a NACA 16-020 type. The generic semi-span wing model has an aspect ratio of 2.3, a semi-span area of 0.683 m², a taper ratio of 0.71 and a 0° sweep of the 50% root chord line. A fan is installed inside the wing rear part (Fig. 2). The model is installed on a peniche to raise the wing out of the wind tunnel wall boundary layer. The rear fan axis position is located at ⅔ of the chord and at 0.12 b from the root chord.

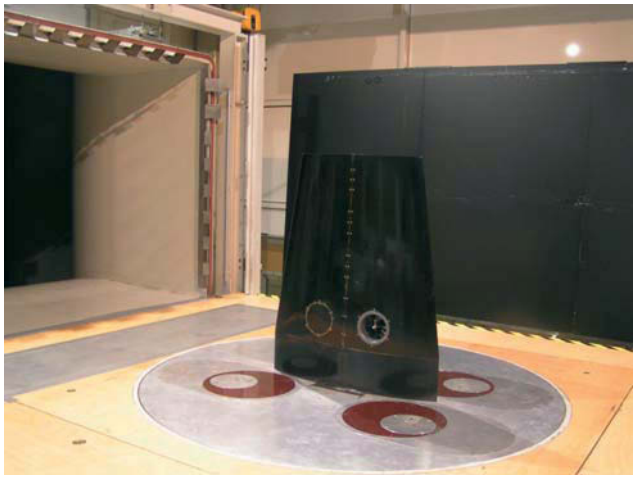

FIG 2. Model in wind tunnel

The fan used during the experiment is originally employed for radio/controlled purpose. It is composed of two stages, a four-blade rotor and four-blade stator. The engine is located inside the stator (Fig. 3a). Further details of the fan geometry are given in Table 1. A constant lip radius to diameter is used over the entire fan circumference (Fig. 3b).

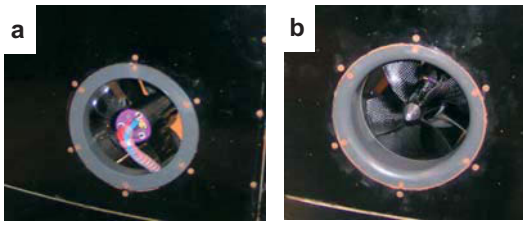

FIG 3. Zoom **a.** on the nozzle, **b.** on the inlet lip

Parameter	Value
Fan diameter /c	0.13
Inlet lip radius to diameter ratio	0.083
Hub-tip ratio	0.42
Rotor blade aspect ratio	0.95
Solidity at hub/tip (rotor)	1.1/0.43
Stagger angle at hub/tip (rotor)	15°/70°
Tip clearance (% span)	1

TABLE 1. Fan specification

2.2. CFD simulations setup

2.2.1. Code description

The flow simulation software ANSYS CFX is used to perform URANS simulations of this fan-in-wing configuration. A second order discretization of the convective terms is used throughout all calculations. The temporal discretization is made using a second order backward Euler scheme. The total energy model is used to account for compressibility effects, particularly significant at the blade tip and on the inlet lip. The k-ω SST turbulence model from Menter [21] is used for all computations. The rotation of the fan is modeled using a sliding mesh approach. A multiblock structured mesh is generated around the geometry with ICEM CFD. The total number of nodes is about 4 millions. The results are time-averaged over a fan period after 5 computed revolutions. A periodicity of the fan coefficients (e. g. thrust, torque) is observed after 3 revolutions. A time history of the fan coefficients is given in Fig. 9. Additional information on the grid and the simulation features can be found in [20]. The influence of the wires providing power (Fig. 3a) to the engine is neglected in the numerical simulation. The fan geometry is simplified to create a suitable blocking around the geometry. The gaps between the rotor and stator and the holes are removed. The rotor blade filets are also neglected. Thus, the blade geometry in the hub vicinity is extrapolated. Despite these changes, the geometry is precisely modeled, including the tip clearance. The surface mesh on the rotor blades is presented in Fig. 4. A satisfactory agreement has been found between the simulations and a wide range of experimental data providing confidence to study the flow at the fan inlet section [20].

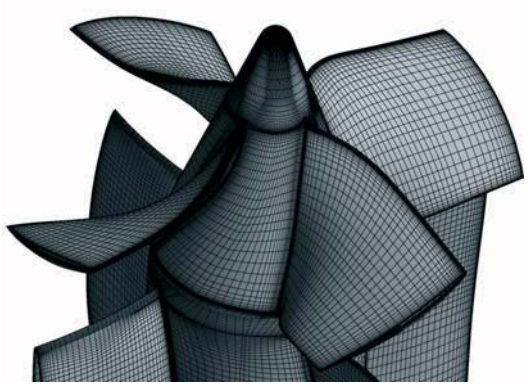

FIG 4. Surface mesh on the rotor blades and hub

As reference, a steady-state simulation of the fan-alone without inlet distortion is performed. Only one blade passage is simulated and periodic conditions are imposed on the sides of the domain to reduce the computational resource requirements. An inlet mass flow condition is imposed in the fan axial direction. The flow coefficient, Φ = 0.87, is identical to the one obtained in the aforementioned URANS simulation. The same node distribution (for the medium grid defined in section 2.2.2), turbulence model and flow properties are used for both simulations. Stage interfaces are used to separate the domain surrounding the rotating rotor blade to the rest of the fluid domain. The stage interfaces average circumferentially the information transferring between the different reference frames and consequently provides a steady state solution [22]. All maximum residuals (turbulence, heat transfer and momentum quantities) are converged to $1x10^{-4}$. A converged solution is obtained in approximately 40 CPU hours for the medium grid (cf. Table 2). Two processors on a 12-nodes Altix cluster are used to carry out the computations of the reference case.

2.2.2. Grid-dependence study

In this section, a grid-dependence study is presented for the reference simulation. Three different meshes are tested: a coarse grid of $4.2x10^5$ nodes, a medium grid (with the same distribution as in the URANS simulation) of $6.2 x10^5$ nodes and a fine grid of $1.1x10^6$ nodes. Relevant dimensions of the grid are given in Table 2. The flow coefficient is ϕ = 0.87 for all simulations.

Parameter (rotor/stator)	**Coarse**	**Medium**	**Fine**
Normal layers	33	38	46
Spanwise layers	55/38	64/44	78/56
Circumferential points	104/128	120/144	148/164
Leading edge spacing /c ($x10^{-3}$)	1.5/1.9	1.3/1.6	1.1/1.4
Trailing edge spacing /c ($x10^{-3}$)	0.5/1.1	0.5/1.1	0.5/1.1
y_+	<1	<1	<1
Total number of nodes	$4.2x10^5$	$6.2x10^5$	$1.1x10^6$

TABLE 2. Details of the grids employed

The solver performs an automatic near wall treatment as the mesh is refined. To benefit from a near wall formulation, the value of y_+ (less than 1) is kept constant on the rotor and stator blades for all grids. The relative difference between the fine and medium grid is about 1% for the pressure rise and thrust coefficient (Table 3). A mesh refinement has a negligible effect on the prediction of the torque coefficient, τ. A grid refinement affects the pressure distribution on the blades surface. A comparison of the static pressure ratio on the rotor blade is presented in Fig. 5. The pressure distribution on the blade is relatively complex but a graphical observation can give some insight on the impact of grid refinement on the fan coefficients. Slight lower pressure is predicted on the upper side of the blade for the fine grid, especially near the blade tip. A graphical evaluation of the pressure distribution also indicates that higher pressure on the blade lower side and on the front part of the blade near the tip for the fine grid. For this reason, higher thrust coefficient and pressure rise coefficient are predicted with the fine grid. The relative difference remains however small. A relatively coarse mesh can therefore be a good

approximation of the pressure rise coefficient, ψ, as well as of the thrust coefficient, C_T, and can therefore be sufficient for achieving a URANS fan-in-wing calculation. Indeed, if the focus is on the wing aerodynamic behavior, a coarse fan grid can give a satisfying prediction of the wing loading at lower computational cost. In the next section, results obtained with the medium grid are compared to the fan-in-wing results.

Parameter	Coarse	Medium	Fine
ψ	0.249	0.255	0.258
τ	0.0102	0.0103	0.0103
C_T	0.339	0.343	0.347

TABLE 3. Comparison of fan coefficients for various grid levels

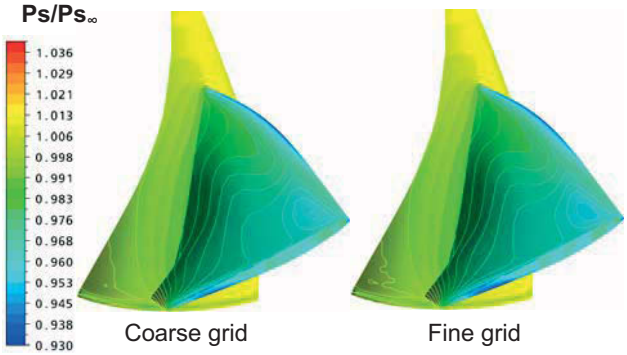

FIG 5. Static pressure ratio distribution on the rotor blade for different grid levels (Φ = 0.87, N = 26,200 rpm)

2.3. Inflow distortion characteristics

In this section, the inflow distortion of the fan-in-wing wind tunnel model is characterized. Axial and circumferential velocities obtained in the URANS simulation are compared to the reference simulation to document the properties of this generic inflow distortion configuration. The angle of attack on the wing is α = 0°, the freestream velocity is 40 m/s, corresponding to $Re_c = 2x10^6$ and the fan rotational speed is N = 26,200 rpm.

2.3.1. Blade dynamic loading

The fan has a strong influence on the flow topology of the wing upper side. This topology is summarized in Fig. 6. Boundary layer separation occurs on the inlet lip and generates a recirculation bubble above the rotor blades.
Figure 7 shows the total pressure ratio distribution at an inlet section located at z/t = 0.3 above the wing camber line. These results are here time-averaged over one fan revolution. Note that the fan rotates counterclockwise as seen from above. The core of the recirculation bubble can clearly be identified by a region of low total pressure ratio. For this fan-in-wing configuration, the major part of the inflow distortion originates from the inlet lip separation. Thus, the total pressure distortion is localized in the front part of the fan inlet. A retreating and advancing flow condition on the rotor blades is responsible for the asymmetric shape of the total pressure distribution.

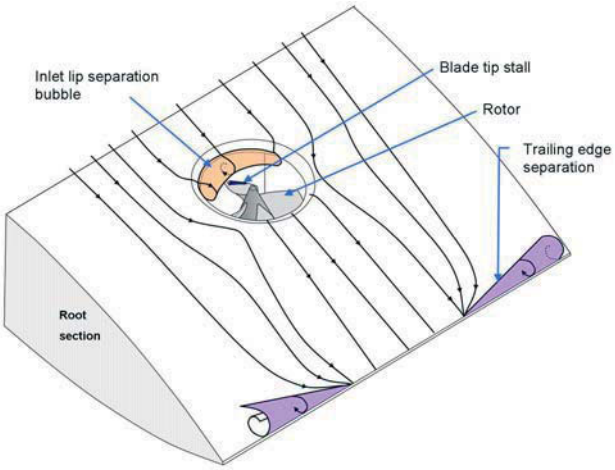

FIG 6. Sketch of the flow topology on the wing upper side

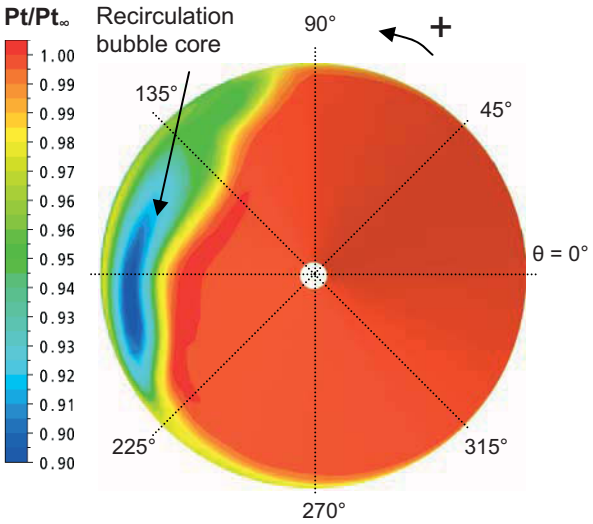

FIG 7. Total pressure ratio distribution above the rotor blades at z/t = 0.3 (V_∞ = 40 m/s, N = 26,200 rpm and α = 0°). The incoming flow direction is left to right.

The time-dependency of the flow, initiated by the fan rotation, induces a significant unsteady behavior of the total pressure distortion at the fan inlet. Reverse flow, characterized by a negative axial velocity component, is observed near the front part of the shroud. Figure 8 shows the static pressure distribution at 70% span in an unwrapped blade-to-blade plane. It is an instantaneous static pressure distribution taken at a given time (therefore at given rotor position). A dynamic loading is observed on the rotor blades consequently inducing significant time variations of the thrust and torque coefficients (Fig. 9). The mean values are C_T = 0.47 and τ = 0.017. The blade element passing in the front part of the inlet section (approximately for 90° < θ < 270° and between 20% to 75% of the span) is subject to a large suction on its upper side. For this reason, a higher loading is observed on this blade thereby generating more thrust than the blade in the region of low total pressure distortion (roughly on the rear part of the inlet section). The static pressure distribution on the blade passing the non-distorted region is similar to the pressure distribution on the blade of the reference

calculation. Therefore, the thrust coefficient is more significant in the fan-in-wing simulation than in the reference case.

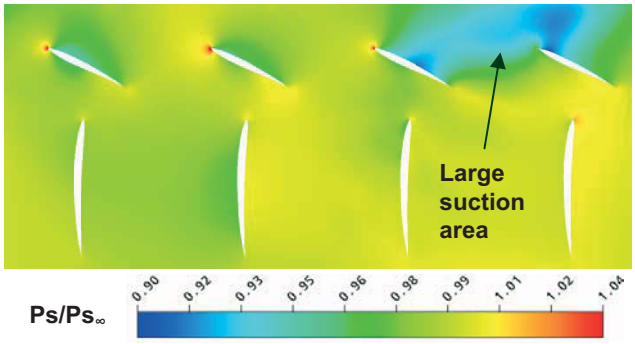

FIG 8. Static pressure ratio distribution at 70% span

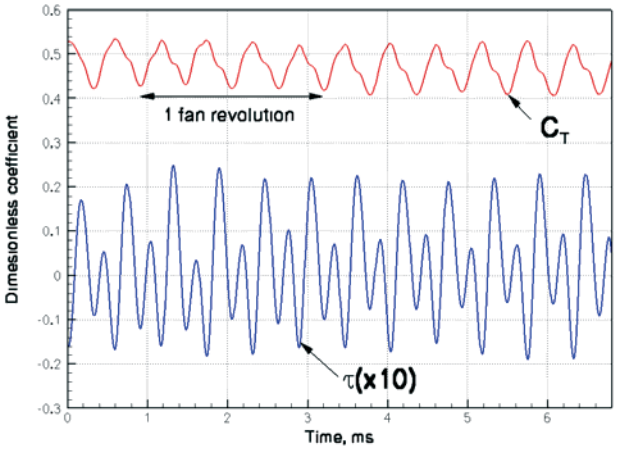

FIG 9. Fan loads variation in time

2.3.2. Velocity distribution

The circumferential distributions, taken at the mid-span position, of the axial and circumferential velocity components are presented in Fig. 10 and compared to the reference case. The transient velocity curve (TRN) is a velocity distribution at a given time (or rotor location). Comparable trends have been observed for the velocity components at other times. It represents the peak-to-peak variation of the axial and circumferential velocity components, respectively. No significant changes are observed in the time-averaged circumferential velocity with respect to the reference solution (Fig. 10a). However the peak-to-peak V_c distribution suggests strong dynamic behavior with a significant increase around θ = 120° and a reduction around θ = 300°. The retreat of the blade results in a significant decrease of V_c in the surrounding flow. Contrary to that, an increase of V_c is observed around the advancing blade. The standard deviation of the circumferential velocity is approximately 15% of the mean value. A positive shift is seen between the time-averaged value of axial velocity component, V_a, and the reference (Fig. 10b). As for the circumferential component, the axial the velocity is characterized by a significant dynamic behavior. The strong velocity gradient occurring above the inlet lip leads to a strong rise of the axial velocity component in the front part of the inlet section and at around mid-span. A maximum of the axial velocity component is located at about θ = 180°. A small area of reduced axial velocity, with respect to the reference value, is present downstream of the hub-cap (-20°<θ<60°). At 50% span, the standard deviation of the axial velocity component represents 24.5% of the mean value. The standard deviation of V_a remains between 16% and 25% of the mean value from 30 to 75% of the blade span. A significant increase of the standard deviation is observed near the shroud, in the recirculation region for all velocity components.

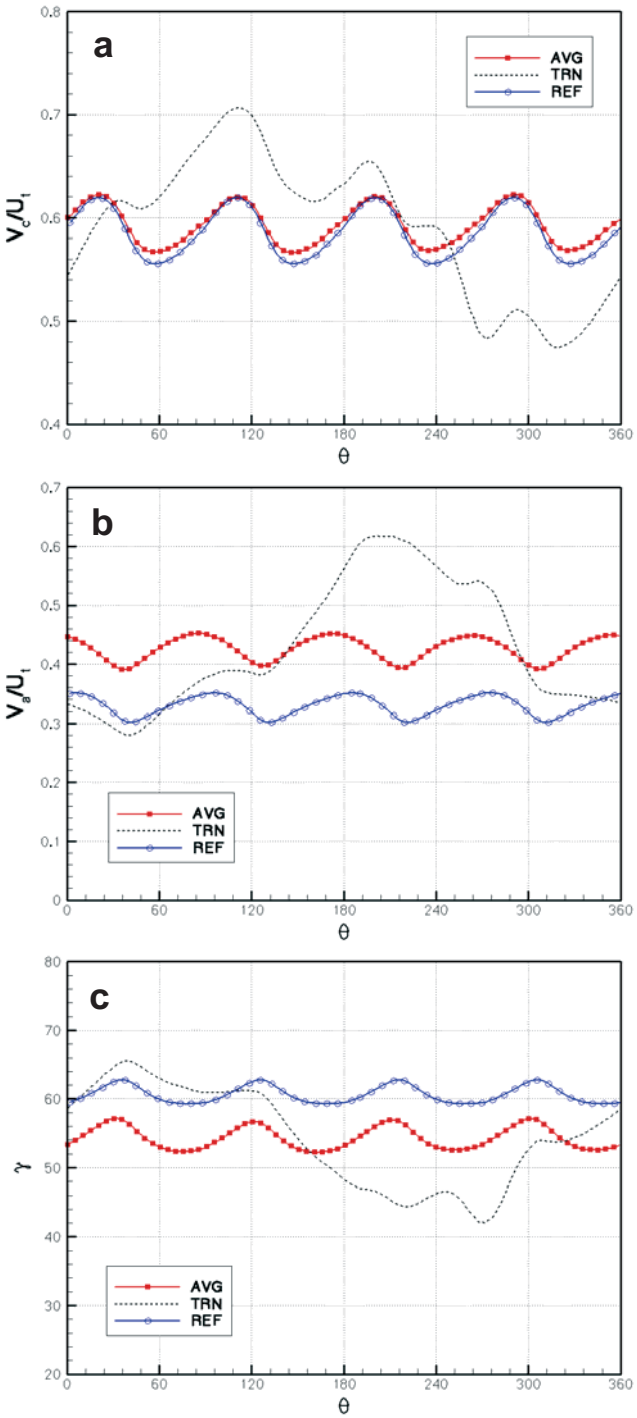

FIG 10. Circumferential distributions at mid span of **a**. circumferential velocity component, **b**. axial velocity component and **c**. swirl angle. (z/t = 0.3, V_∞ = 40 m/s, N = 26,200 rpm and α = 0°)

The variations in the axial and circumferential velocity components have an impact on the swirl angle and therefore on the blade incidence angle. A negative shift is observed between the time-averaged swirl angle and the reference swirl angle at mid-span (Fig. 10c). The strong increase of the axial velocity component around θ = 180° results in a significant reduction of the swirl angle and therefore in a decrease of the incidence angle on the blade. Note that for 0<θ<60°, the swirl angle slightly increases due to an increase of V_c combined with a reduction of V_a.

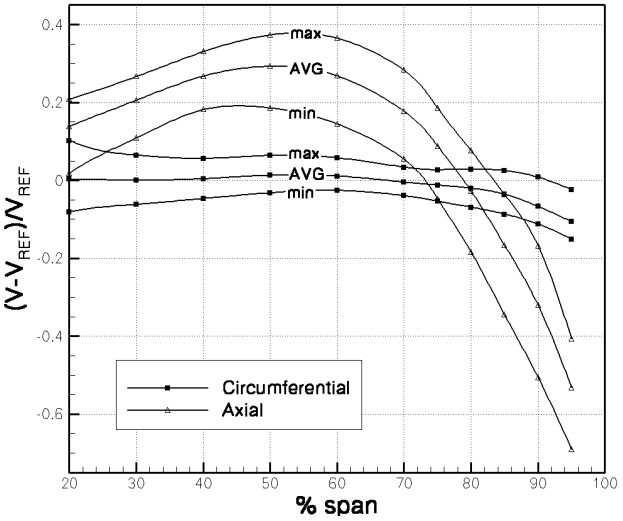

FIG 11. Relative velocity component magnitude as function of the blade spanwise position (z/t = 0.3, V_∞ = 40 m/s, N = 26,200 rpm and α = 0°)

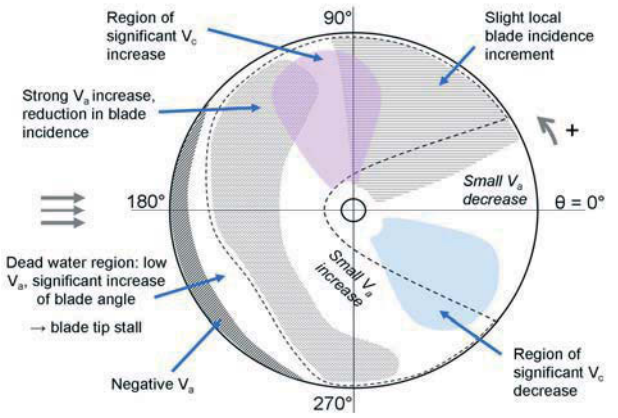

FIG 12. Sketch of the inlet section velocity distribution

Figure 11 represents the variation of the time-averaged velocity to the reference steady state velocity at various blade span positions. The values are averaged circumferentially for a given blade span location. The relative circumferential velocity remains fairly constant along the entire span. Near the shroud, however, a slight decrease of the relative circumferential velocity is observed. The maximum relative axial velocity is obtained around mid-span due to the large flow velocity gradient occurring over the inlet lip. The relative axial velocity considerably drops in the vicinity of the shroud inside the recirculation bubble core.

To summarize these findings, the wing incoming boundary layer separates on the inlet lip and generates a recirculation bubble at the fan inlet. Reverse flow is observed on the front part of the shroud. The core of the recirculation bubble is characterized by low pressure, small axial velocity component and therefore large blade incidence which induces blade tip stall. Downstream of the bubble core, the axial velocity component is considerably increased and consequently the blade incidence angle is reduced. Compared to the reference, an increase of the circumferential velocity component occurs near the advancing blade whereas V_c decreases in the flow surrounding the retreating blade (Fig. 12).

3. DISTORTION PARAMETERS

Unsteady computations of the complete fan-in-wing configuration require significant computational resources. Replacing the fan by an actuator disk contributes to reduce the computational costs, necessary for a parametric study. The key parameters affecting the inflow distortion, characterized in section 2, are reported to provide additional design sensitivities.

3.1. Setup

As sketched in Fig. 13, the fan is removed from the geometry and substituted by boundary conditions at the fan inlet and exit. On the disk upper side an outlet boundary condition is imposed with a uniform axial velocity profile. On the disk lower side, an inlet boundary condition is set with the same uniform axial velocity distribution. The turbulent intensity prescribed is 7% according to the URANS simulation.

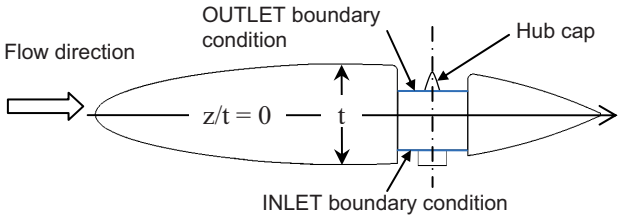

FIG 13. Schematic view of the “actuator disk” setup.

Steady Reynolds Averaged Navier-Stokes calculations are conducted using the k-ω SST turbulence model similarly as in the aforementioned URANS calculations. The spatial discretization remains as in section 2.2. The residual convergence depends on the velocity ratio. In most cases max-residuals are converged to $1x10^{-4}$. For $V_\infty/V_j > 1$ and $V_\infty/V_j < 0.5$, unsteady flow tendency limits the maximum residuals convergence between 10^{-3} and 10^{-4}.

A structured mesh is constructed around the geometry. Details of the grid employed are given in table 4. Results obtained with this actuator disk approach have been compared to experimental data and to time averaged URANS results. A satisfactory agreement has been found. The actuator disk setup gives a good prediction of the mass flow through the fan as well as of the pressure rise coefficient. Therefore, the flow topology and the pressure distribution on the wing (Fig. 14) are well represented. Further details on the comparison can be found in ref. [23]. The outlet boundary condition is placed sufficiently far away from the inlet observation section and affects slightly the lip flow separation compared to the URANS simulation results. This actuator disk approach does not account for a

retreating and advancing flow condition due to the fan rotation. However, this representation of the fan provides a simple way to investigate the major parameters affecting the inlet distortion of a fan-in-wing configuration. Grid refinements in various directions have been realized. Small changes have been observed on the results. Therefore, all computations are performed with the grid described in table 4. The surface mesh on a plane cutting the fan center is showed in Fig. 15.

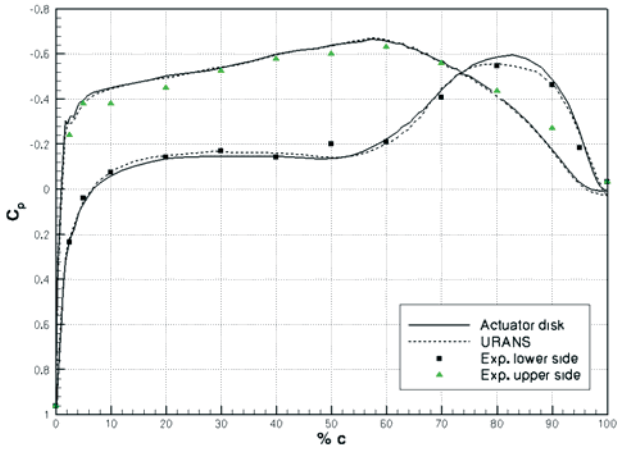

FIG 14. Chordwise pressure distribution on the wing at 1/3 b from the root chord (N = 26200 rpm, V_∞ = 40 m/s, and α = 0°)

Parameter	Value
Wrap-around points	200
Leading edge spacing / c	3×10^{-3}
Trailing edge spacing / c	5×10^{-4}
Inlet lip spacing / r_{lip}	0.083
Total number of nodes	1.4×10^{6}

TABLE 4. Details of the grid.

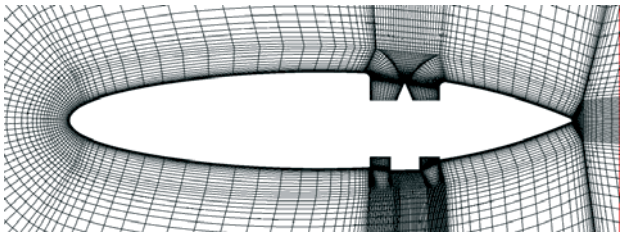

FIG 15. Surface mesh at the fan middle plane

3.2. Effect of the lip radius to diameter ratio

Increasing the value of the inlet lip radius to diameter contributes to diminish the suction peak on the inlet lip and thereby reduces the adverse pressure gradient. Consequently the relative location (angular position on the lip, θ_v) of the separation line on the curved inlet is displaced downstream. The spatial extension of the recirculation bubble is considerably reduced. Thus, increasing the inlet lip radius to diameter ratio reduces the total pressure inflow distortion (Fig. 16). The swirl distortion is therefore decreased due to a lower axial velocity component in the front part of the inlet section. The fan has to be housed compactly inside the wing to obtain satisfying cruise performance. Consequently, the value of lip radius to diameter is limited by design constraints. A specific inlet lip design with a variable lip radius to diameter remains an alternative to decrease the inflow total pressure distortion.

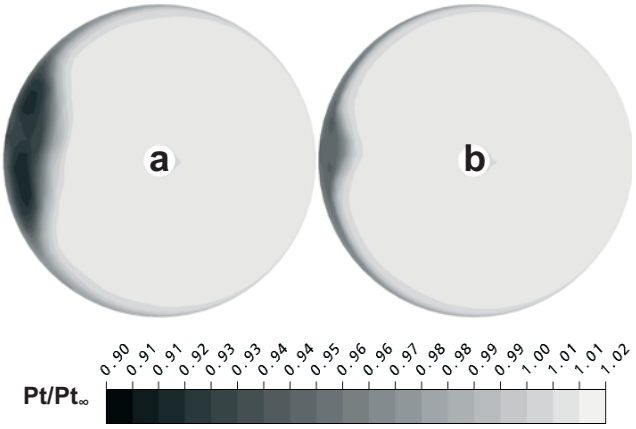

FIG 16. Total pressure coefficient contours at the fan inlet a. 8.3% and 16.7% lip radius to diameter ratio (z/t = 0.3, V_∞ / V_j = 0.65, and α = 0°)

3.3. Effect of the velocity ratio

The velocity ratio, V_∞/V_j, has a strong influence on the total pressure ratio distribution at the fan inlet. V_∞/V_j accounts indirectly for the fan rotational speed and could be replaced by the tip-speed ratio. A decrease of V_∞/V_j (therefore an increase of the jet velocity and the mass flow through the fan) results in a displacement of the separation line on the front part of the inlet lip. As V_∞/V_j is reduced, the separation point at the fan center line moves downstream (Fig. 17). Accordingly, the stagnation region on the rear part of the inlet lip is pushed downstream. At higher jet speed, the stagnation area is located downstream of the inlet lip, causing significant lift penalty on the wing. The size of the recirculation bubble increases with increasing V_∞/V_j (Fig. 18). The parameter l_{max} represents the maximum radial extension of the recirculation bubble measured from the shroud as indicated in Fig. 18. As the velocity ratio is reduced, the size of the bubble is significantly enhanced. l_{max} varies allmost linearly with respect to the velocity ratio.

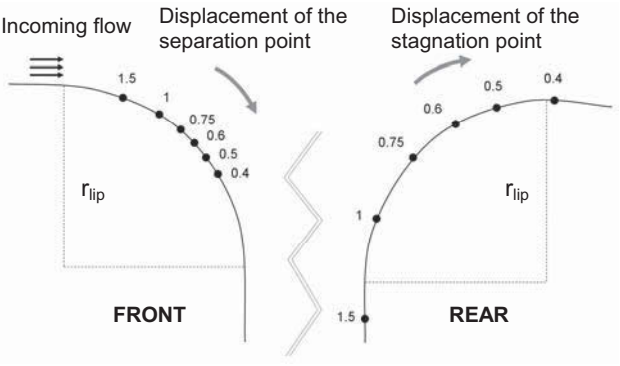

FIG 17. Relocation of the separation and stagnation point with respect to a decrease of the velocity ratio at the fan center line (α = 0°)

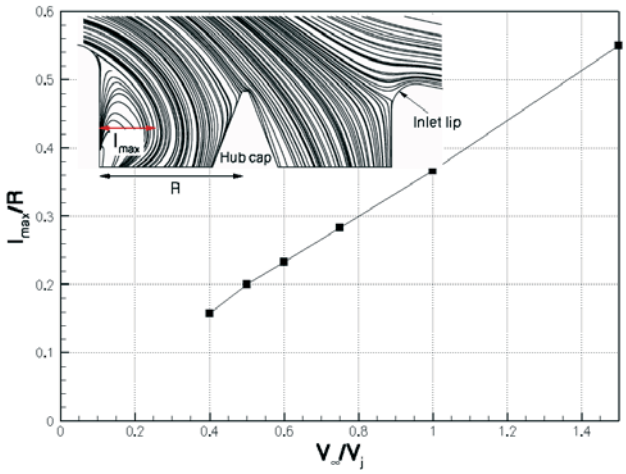

FIG 18. Influence of the velocity ratio on the radial extension of the inlet lip separation bubble (α = 0°)

The circumferential extension of the recirculation bubble is also affected by a variation of the velocity ratio. As the jet velocity decreases, the circumferential extension of the bubble is enhanced. The total pressure ratio distribution taken at the fan center line is shown in Fig. 19 and characterizes the inflow pressure distortion. An increase of the mass flow through the fan results in a higher velocity gradient over the inlet lip. Consequently, a larger suction peak is generated in the front part of the fan inlet. Due to the large separation bubble created at high V_∞/V_j, the pressure gradient is reduced from the shroud to the hub. The major part of the circumferential extension of the flow distortion is within θ = 135° to θ = 225°.

Summarizing, increasing the jet speed reduces the radial and circumferential extension of the recirculation bubble. However, the total pressure inflow distortion is locally increased, near the front part of the inlet section, due to a strong suction caused by a large velocity gradient over the inlet lip.

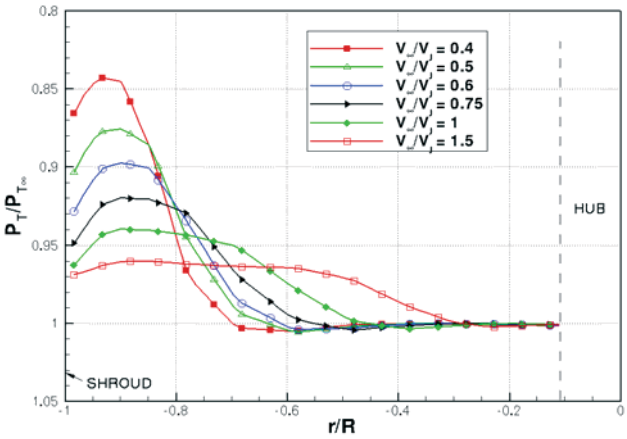

FIG 19. Radial pressure distribution at the fan inlet section center line (z/t = 0.3, α = 0°)

3.4. Effect of the angle of attack

A change of the angle of attack has a negligible impact on the total pressure distribution at the fan inlet as far as the flow remains attached. Downstream of its inlet, the fan maintains the flow attached at the trailing edge at α = 0° (Fig. 6). The trailing edge separation extends upstream as the wing angle of attack is increased. However, no trailing edge separation is observed in the region downstream of the fan below α = 20° [19].

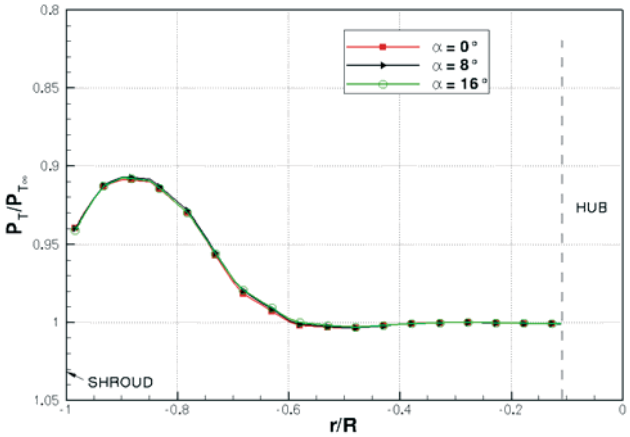

FIG 20. Radial pressure distribution at the fan inlet section center line (z/t = 0.3, V_∞/V_i = 0.65)

The radial total pressure distribution (Fig. 20) at the fan middle line confirms this conclusion. The boundary layer separation on the inlet lip is not affected by a variation of the angle of attack. The radial and circumferential extension of the separation bubble is consequently similar for all α investigated. The stagnation area located on the rear part of the inlet lip remains also unchanged with respect to a variation of angle of attack. Radial and circumferential distributions at the fan inlet are consequently unchanged. The previous conclusions hold if the wing is not stalled. According to [19], stall occurs at about α = 26° resulting in fan surge.

3.5. Effect of an inlet guide vane

As previously stated, the characteristics of the recirculation bubble generated above the fan strongly depend on the velocity ratio. An active lip-flow control device can contribute to reduce the inflow distortion, and requires to be adjusted to the operating conditions. A configuration with an inlet guiding vane (IGV) positioned near the inlet lip is investigated for this purpose (similarly, boundary layer control slats are used in ref. [17]).

In this section, 2D calculations are performed to provide IGV design sensitivity at cheap computational cost. The 2D domain investigated corresponds to a cut of the 3D domain at the fan center. A 2D representation does not account for any 3D effects that would be observed in an actual fan-in-wing arrangement with IGV (e. g. retreating and advancing flow condition, pressure gradient along the IGV span, sideslip angle on the IGV element, spanwise pressure gradient on the wing). However, at the fan center, the effect of an IGV on the flow over the inlet lip and particularly its influence on the separation bears strong similarities with a 2D simulation. This statement has been verified for a 3D actuator disk calculation including a 90°-extension IGV located at the front part of the inlet section. Numerous parameters are necessary to describe the position of the IGV with respect to the inlet lip (Fig. 21). As a first step of an IGV design, 2D simulations have been preferred to highlight the major effects induced by a guide vane on the flow near the inlet lip. A 3D investigation,

more costly, of the IGV with an actuator disk approach would then be an essential second step for the IGV design.

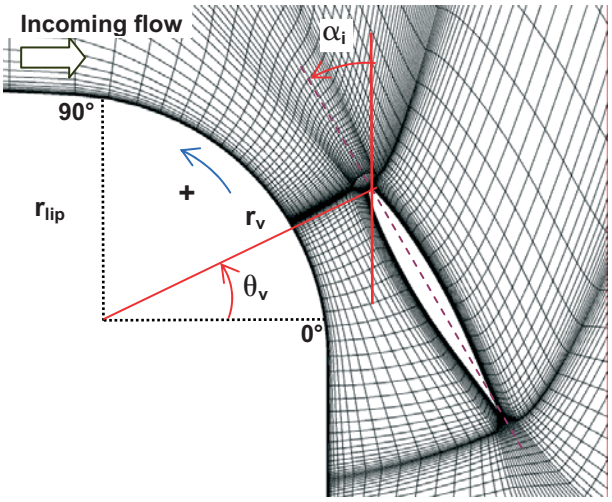

FIG 21. IGV coordinate system superimposed on surface mesh

The IGV airfoil is of NACA 65-010 type, also used as in ref. [16]. The guide vane chord to lip radius is 1. The leading edge of the guide vane is located at a distance r_v and at an angle θ_v from the lip center of curvature. In the entire section, the radial distance of the IGV to the center is kept constant, $r_v / r_{lip} = 1.2$.

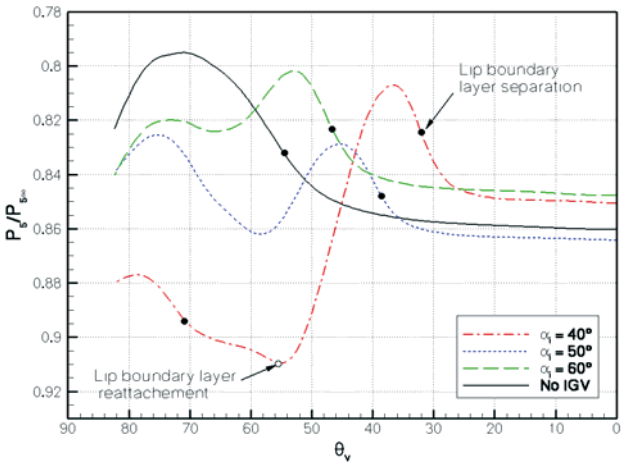

FIG 22. Circumferential static pressure ratio distribution for several IGV duct inlet vane angle (V_∞ / V_j = 0.5, α = 0°, the IGV leading edge is located at θ_v = 60°)

For the case without IGV, downstream of the suction peak (around θ_v = 75°), an adverse pressure gradient provokes the separation of the lip boundary layer at about θ_v = 54° (Fig. 22). Introducing an IGV near the inlet lip induces a secondary pressure peak due to a significant increase of flow velocity near the vane leading edge. The adverse pressure gradient causing boundary layer separation on the lip is therefore delayed. As α_I is reduced, the separation on the inlet lip moves downstream. However, for α_I < 40°, the inlet lip boundary layer separates upstream of the IGV. The negative pressure gradient occurring downstream reattaches the boundary layer on the lip. The IGV contributes to increase the velocity near the inlet lip and re-energizes the boundary layer. Therefore, the separation on the inlet lip is delayed downstream compared to the case without guide vane. Inlet lip flow separation can be avoided for a small α_I but massive separation occurs on the guide vane upper side (Fig. 23). Therefore, the problem is moved from the inlet lip to the IGV. Note that in Fig. 23, the legend indicates the angular position of the IGV leading edge. The parameter $\Delta\theta_v$ represents the angular displacement of the separation point on the inlet lip.

An opposite trend is observed for an IGV leading edge positioned at θ_v = 30°. For α_I < 40°, the IGV has a negligible influence on the inlet lip separation. For low duct vane angle, massive separation on the IGV upper side is combined to the lip separation bubble. As α_I increases, the effective angle of incidence on the IGV decreases. For α_I > 54°, the flow remains attached on the inlet lip (Fig. 24). A negative angle of incidence on the IGV provokes a large suction peak on the lower side of the guide vane. A significant velocity enhancement near the lower side of the IGV leading edge re-energized the inlet lip boundary layer. However, a large recirculation bubble is generated on the IGV lower side. The origin of inflow distortion is also transferred from the lip to the IGV lower side. The IGV increases the mass flow rate near the inlet lip with respect to the case without guide vane. For a large α_I, the velocity is locally increased only near the IGV leading edge and decreases rapidly as the relative distance between the IGV and the inlet lip is rising. A cambered guide vane along the inlet lip can maintain the flow attached on a larger portion on the inlet lip. The airfoil section and the duct inlet vane angle (therefore the effective IGV angle of incidence) have to be carefully selected to avoid massive separation on the IGV. Here, the small radius of curvature requires setting the IGV with a significant effective incidence angle to maintain attached flow along the lip. Therefore a situation with attached flow on both inlet lip and guide vane has not been achieved within the range of calculations conducted. An inlet guide vane located near the inlet lip remains a complex solution to control the lip separation and therefore the total pressure distribution at the fan inlet section. However, combining the inlet lip design and the guide vane can be a suitable solute on for passive and active lip flow control, respectively.

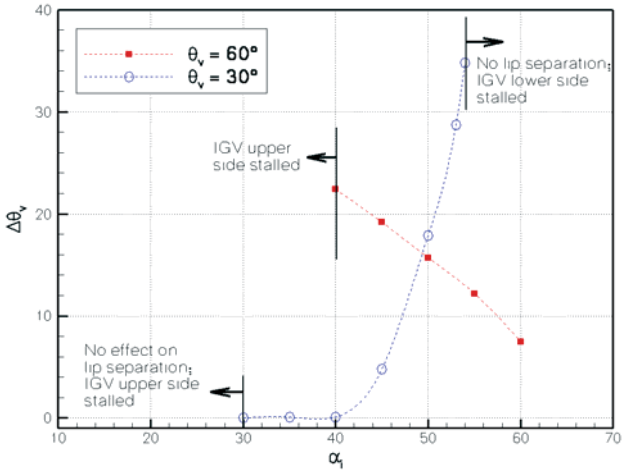

FIG 23. Circumferential variation of the angular separation point location for various duct inlet vane angles (V_∞ / V_j = 0.5, α = 0°)

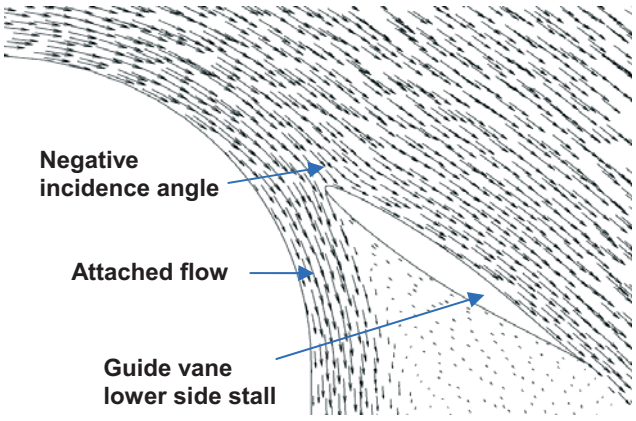

FIG 24. Velocity vector distribution around the inlet guide vane (V_∞ / V_j = 0.5, α = 0°, α_i = 55°). The IGV leading edge is set as θ_v = 30°.

3.6. Lip-separation control via injection

An inlet guide vane remains a complex solution to control the boundary layer on the inlet lip. Concepts to control actively the flow of an airfoil (e. g. blowing, suction) can be applied to the present configuration. A lift improvement can also be achieved by blowing on the cambered inlet lip and exploiting the Coanda effect. In this section, a 2D calculation is performed with a blowing slot upstream of the inlet lip (located at θ_v = 90°) to demonstrate the capability of such a flow control solution to maintain attached flow on the inlet lip. No particular optimization has been realized on the blowing slot. The slot height is here 2.5 x 10^{-2} r_{lip}. The slot-jet momentum coefficient is about 0.02. Without blowing, separation occurs on the inlet lip and generates a recirculation bubble above the fan (Fig. 25a). Contrary, lip separation is avoided with the presence of a wall jet blown from the slot (Fig. 25b). In addition, the flow entering the fan is more effectively turned. The swirl angle and the air ingestion at the fan inlet are improved with a blown-lip device.

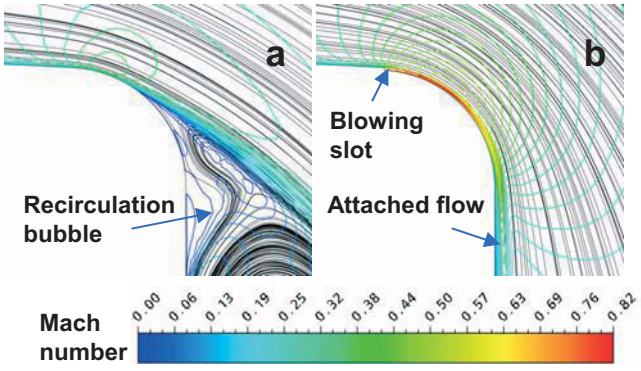

FIG 25. Mach number contours superimposed with streamlines (V_∞ / V_j = 0.67, α = 0°).

4. CONCLUSION AND OUTLOOK

The aerodynamic characteristics of a lift-fan under inflow distortions in the form of a generic fan-in-wing configuration have been studied. The total pressure and the velocity distributions at the fan inlet have been analyzed by comparing results of Unsteady Reynolds Averaged Navier-Stokes computations to steady results of the fan-alone without inlet distortion. The main parameters influencing this specific inflow distortion configuration have been documented using an actuator disk approach. The major conclusions are as follows:

1) The main part of inflow distortion originates from the separation of the wing boundary layer on the inlet lip which generates a recirculation bubble above the rotor blades. In the front part of the inlet section around mid-span, the axial velocity component is strongly enhanced compared to the reference case without inlet distortion. This results in a decrease of the swirl angle as well as the blade incidence angle. In the bubble core, low axial velocity component induces a large local blade incidence angle. Therefore, the rotor is subject to blade tip-stall in this region. The dynamic behavior of the distortion is significant and impacts on the blade loading.
2) The ratio of the freestream velocity to the jet velocity notably affects the separation on the inlet lip and therefore the total pressure distortion at the fan inlet. Increasing the ratio of inlet lip radius to diameter contributes to reduce the pressure gradient on the inlet lip and delays the lip separation resulting in a less distorted inflow. The angle of attack on the wing has negligible influence on the total pressure distribution at the fan inlet.
3) An inlet guide vane located near the inlet lip can be an alternative to control lip flow separation. Compared to a case without guide vane, the vane re-energizes the inlet lip boundary layer and shifts downstream the lip separation location. Depending on the vane effective incidence angle, lip separation can be suppressed but massive separation can occur on one side of the guide vane. The guide vane requires particular attention to be adjusted. The source of the distortion is otherwise transferred from the lip to the vane.
   Active airfoil flow control solutions can be implemented to the inlet lip boundary layer. Blowing a wall jet on the inlet lip can maintain attached flow and can improve the air ingestion at the fan inlet section.

Additional work will be carried out on the design of an inlet lip with variable lip radius to diameter. Further two-dimensional calculations will then be conducted to select a suitable guide vane and to increase the design sensitivity of a blown-lip solution. Finally, 3D effects of an active flow control device on the inflow distortion will be investigated.

Acknowledgment

The authors would like to thank ANSYS CFX for providing the flow simulation software and Mr. Schübeler for the fan CAD data. The support of these investigations by the Bauhaus Luftfahrt e. V. is gratefully acknowledged.

References

[1] Gologan, C., Heister, C., Kelders, C., Kuhlmann, A. and Seifert, J., Perspective of Vertical / Short Take Off and Landing in Commercial Aviation, *Proceedings of the CEAS Air and Space Conference*, Sept. 2007, Berlin, Germany
[2] Hirschberg, M. J., An Overview of the History of Vertical and/or Short Take-Off and Landing (V/STOL)

Aircraft,
http://www.vstol.org/history_overview_brief.pdf

[3] Jahren, W., Peters, T. and Fottner, L., An experimental flow investigation of an HP Five-Stage Compressor Exhibiting Rotating Stall due to Distorted Inlet Flow Conditions, *Unsteady Aerodynamics and Aeroelasticity of Turbomachines*, pp. 243-257, 1998

[4] Hah, C., Rabe, D. C., Sullivan, T. J. and Wadia, A. R., Effects of Inlet Distortion on the Flow Field in a Transonic Compressor rotor, *Journal of Turbomachinery*, Vol. 120, pp. 233-246, 1998

[5] Yao, J., Gorrell, S. E. and Wadia, A. R., A Time-Accurate CFD Analysis of Inlet Distortion Induced Swirl in Multistage Fans, *Proceedings of the Joint Propulsion Conference and Exhibit*, AIAA 2007-5059, July 2007, Cincinnati, OH, USA

[6] Jang, C-M., Choi, S-M. and Kim, K-Y., Effect of Inflow Distortion due to Hub Cap´s Shape on the Performance of Axial Flow Fan, *Journal of Fluid Science and Technology*, Vol. 3, No. 5, pp. 598-609, 2008

[7] Abott, J. M. and Dietrich, D. A., Aerodynamic and Directional Acoustic Performance of a Scoop Inlet, NASA TP 1028, Sept. 1977

[8] Smith, C. F., Podleski, S. D., Barankiewicz, W. S. and Zeleznik, S. Z., Evaluation of F/A-18A HARV Inlet Flow Analysis with Flight Data, NASA TM-107130, Dec. 1995

[9] Syberg, J., Low Speed Test of a High-Bypass-Ratio Propulsion System with an Asymmetric Inlet Designed for a Tilt-Nacelle V/STOL Airplane, NASA CR-152072, Jan. 1978

[10] Sylvester, T., Brown, R., Moore, S., Thorne, G. and Priesley, J, F-35 STOVL Lift Fan Inlet Development and Lessons Learned, *Proceedings of the International Powered Lift Conference*, July 2008, London, UK

[11] Krishnappa, G., Liftting Fan Noise Studies with Superimposed Cross Flows, *Journal of Aircraft*, Vol. 9, No. 10, pp. 719-725, 1972

[12] Shaub, U. W., Experimental Investigation of Flow Distortion in Fan-in-Wing Inlets, *Journal of Aircraft*, Vol. 5, No. 5, pp. 473-478, 1968

[13] Kirk, J. V., Hickey, D. H. and Hall, L. P., Aerodynamic Characteristics of a Full-Scale Fan-in-Wing Model Including Results in Ground Effect with Nose-Fan Pitch Control, NASA TN D-2368, July 1964

[14] Kirby, R. H. and Chambers, J. R., Flight Investigation of Dynamic Stability and Control Characteristics of a 0.18-Scale Model of Fan-in-Wing VTOL Airplane, NASA TN D-3412, Aug. 1966

[15] Hodder, B. K., Kirk, J. V. and Hall, L. P., Aerodynamic Characteristics of Large-Scale Model with a Lift-Fan Mounted in a 5-percent-thick Triangular Wing, Including the Effects of BLC on the Lift-Fan Inlet, NASA TN D-7031, Dec. 1970

[16] Hickey, D. H. and Ellis, D. R., Wind-Tunnel Tests of a Semispan Wing with a Fan Rotating in the Plane of the Wing, NASA TN D-88, Oct. 1959

[17] Gregory, N. and Love, E. A., Wind Tunnel Tests on a Nacelle fitted with two Lifting Fans in Tandem, *Aeronautical Research Council Reports and Memoranda*, R. & M. No. 3494, 1967

[18] Soranna, F., Chow, Y-C., Uzol, O. and Katz, J., The effect of Inlet Guide Vanes Wake Impingement on the Flow Structure and Turbulence around a Rotor Blade, *Journal of Turbomachinery*, Vol. 128, pp.82-95, 2006

[19] Thouault, N., Breitsamter, C., Adams, N. A., Gologan, J. and Seifert, J., Experimental Investigation of the Aerodynamic Characteristics of Generic Fan-in-Wing Configurations, *the Aeronautical Journal*, Vol. 113, No. 3338, 2009

[20] Thouault, N., Breitsamter, C. and Adams, N. A., Numerical and Experimental Analysis of a Generic Fan-in-Wing Configuration, *Journal of Aircraft*, Vol. 42, No. 2, pp- 2009

[21] Menter, F. R., Two-Equation Eddy-Viscosity Turbulence Model for Engineering Applications, *AIAA Journal*, Vol. 32, pp. 1598-1605, 1994

[22] Ansys, Ansys CFX-Solver Theory Guide, Release 11.0, pp. 119-121, Dec. 2006

[23] Thouault, N., Breitsamter, C., Gologan, C., Adams, N. A., Numerical Analysis of Design Parameters for a generic fan-in-wing configuration, *Proceedings of the CEAS Air and Space Conference,* Oct. 2009, Manchester, UK.